August 2001 • NREL/SR-520-30870

Subcontractor Report

In-Situ Sensors for Process Control of CuIn(Ga)Se_2 Module Deposition

Final Report
August 15, 2001

I.L. Eisgruber
ITN Energy Systems, Inc.
Littleton, Colorado

National Renewable Energy Laboratory

1617 Cole Boulevard
Golden, Colorado 80401-3393

NREL is a U.S. Department of Energy Laboratory
Operated by Midwest Research Institute • Battelle • Bechtel

Contract No. DE-AC36-99-GO10337

August 2001 • NREL/SR-520-30870

In-Situ Sensors for Process Control of CuIn(Ga)Se_2 Module Deposition

Final Report
August 15, 2001

I.L. Eisgruber
ITN Energy Systems, Inc.
Littleton, Colorado

NREL Technical Monitor: H.S. Ullal

Prepared under Subcontract No. ZAK-8-17619-08

National Renewable Energy Laboratory

1617 Cole Boulevard
Golden, Colorado 80401-3393

NREL is a U.S. Department of Energy Laboratory
Operated by Midwest Research Institute • Battelle • Bechtel

Contract No. DE-AC36-99-GO10337

NOTICE

Available electronically at http://www.doe.gov/bridge

Available for a processing fee to U.S. Department of Energy
and its contractors, in paper, from:

U.S. Department of Energy
Office of Scientific and Technical Information
P.O. Box 62
Oak Ridge, TN 37831-0062
phone: 865.576.8401
fax: 865.576.5728
email: reports@adonis.osti.gov

Available for sale to the public, in paper, from:

U.S. Department of Commerce
National Technical Information Service
5285 Port Royal Road
Springfield, VA 22161
phone: 800.553.6847
fax: 703.605.6900
email: orders@ntis.fedworld.gov
online ordering: http://www.ntis.gov/ordering.htm

Printed on paper containing at least 50% wastepaper, including 20% postconsumer waste

TABLE OF CONTENTS

LIST OF TABLES

LIST OF FIGURES

1. Introduction

Yield and reproducibility issues remain an important challenge in the manufacture of $Cu(In,Ga)Se_2$ (CIGS) photovoltaic modules. Although champion cells report impressive efficiencies, reproducing these efficiencies in large numbers and over large areas remains problematic. The difficulty of maintaining high yields is compounded when manufacturing throughput requirements are imposed on the deposition process. Development of real-time sensors for processing is therefore an important step towards realizing the potential of CIGS modules for cheap, large-scale power production. Real-time sensors help realize this potential in several manners: First, they allow process conditions to be corrected as they begin to move out of the optimum range, *before* yield is affected. Second, they allow documentation of the deposition conditions producing various qualities of devices, aiding the optimization of conditions and prevention of lost processes. Finally, they provide real-time information about deposition system behavior, furthering the operator's understanding of the deposition system's thermal and transient behavior.

Several different sensors for CIGS module fabrication were examined under this contract. The largest portion of the research and development involved the implementation of an in-situ composition sensor for CIGS deposition. An in-situ composition sensor based on x-ray fluorescence (XRF) was developed. Initial analysis and equipment development was performed ex-situ (post-deposition). Then, hardware allowing installation of the XRF sensor in the CIGS deposition environment was developed. XRF sensors were installed in CIGS production roll-coaters at industrial partner Global Solar Energy, LLC (GSE), and are currently being used in real-time control. Also, the applicability of XRF sensors to other layers in CIGS modules was assessed. Second, non-contact infrared (IR) thermometry was developed for substrate temperature and emissivity measurement during CIGS deposition. Certain portions of demonstrating the in-situ, low-cost, IR thermometer remain as future work. Finally, some effort was also expended to evaluate the use of optical emission spectroscopy (OES) in the deposition of various materials used in CIGS modules.

The work described in this report commenced at Materials Research Group, Inc. (MRG). The contract was transferred to ITN Energy Systems, Inc. (ITN) upon close of business at MRG. This report describes the entire body of work relevant to this contract, performed both at MRG and at ITN.

2. Ex-Situ XRF Development

2.1 Introduction to X-Ray Fluorescence

X-ray fluorescence measurements are performed by illuminating a portion of the sample with x-rays and then measuring the energy and count rate of the fluoresced x-rays. Incident x-ray photons cause electrons to be ejected from atoms in the sample. As the remaining electrons fill the newly-created vacancies by relaxing back to the ground state, excess energy from the relaxing electrons is emitted in the form of x-rays. The energy of these fluoresced x-rays corresponds to the energy change of the electron transition, and therefore each element fluoresces at a characteristic set of x-ray energies. The amount of any element present is related to the strength of the emissions at its characteristic energies. X-rays resulting from the most probable transitions terminating in the K shell are known as "Kα" x-rays. Here "K" signifies the shell at which the transition ends, and "α" signifies that the transition started in the quantum mechanically most probable energy shell. Similarly, x-rays resulting from the most probable transitions terminating in the L shell are known as "Lα" x-rays. Higher energy incident x-rays are required to cause K fluorescence than to cause L fluorescence, as the electron vacancies allowing K fluorescence require more energy to create. Fluorescence occurring due to direct excitation by x-rays from the x-ray source is termed

"primary fluorescence". Fluorescence occurring due to excitation by primary fluorescence is termed "secondary fluorescence".

Typical XRF systems are installed as an accessory on scanning electron microscopes (SEM's), or as self-contained desktop and portable units for soils and metals analysis.[1,2] XRF in itself is not a new measurement; however, a number of the features of the XRF measurement and analysis shown in this report *are* novel. Novel elements of the XRF hardware include protection of the sensor from the deposition environment, use of a sensor-to-sample distance appropriate to deposition chambers, and the use of only low-cost components operating at room temperature. Novel aspects of the XRF analysis include one-sample calibration that gives valid results over a wide range of compositions, real-time CIGS analysis, and compensation for variations in substrate location and x-ray tube current drift by using the substrate signal. The application of XRF to CIGS deposition allows the use of innovative hardware and analysis because the elements present in the film are known prior to measurement, samples are large, 1% precision is sufficient, and recent advances in x-ray tube and detector manufacture have occurred.

2.2 Equipment

XRF measurements require the choice of an appropriate x-ray source, measurement geometry, x-ray detector, detection electronics, and analysis routines. The x-ray source energy and intensity must be chosen so that all elements of interest are excited with sufficient intensity for the desired measurement accuracy. Figure 1 shows the calculated primary fluorescence sample yield for a 2.5 μm CIGS sample as a function of incident x-ray energy. The primary emission energies of several x-ray source anode materials are shown as vertical lines in Figure 1. Measurement geometry must be chosen so that count rate is sufficient, and so that only x-rays fluoresced from the sample are measured. Count rate decreases with a $\frac{1}{r_s^2}$ dependency on the distance from the x-ray source to the sample, and an additional $\frac{1}{r_d^2}$ dependency on the distance from the sample to the x-ray detector. X-ray spot size and detector view areas can be controlled through the use of collimators and apertures. For in-situ monitoring, fluoresced x-ray energies and rates should be measured with a solid-state energy-dispersive detector. X-rays are absorbed in the detector and create a current pulse, proportional to the x-ray energy. These pulses are amplified and then counted with a multichannel analyzer. In some XRF applications, wavelength-dispersive detection is employed, where a rotating crystal diffracts x-rays of a given wavelength to a fixed detector. Wavelength-dispersive detection provides superior energy resolution and maximum count rate; however, the required measurement time and the geometry of the diffraction apparatus is prohibitive for in-situ composition monitoring.

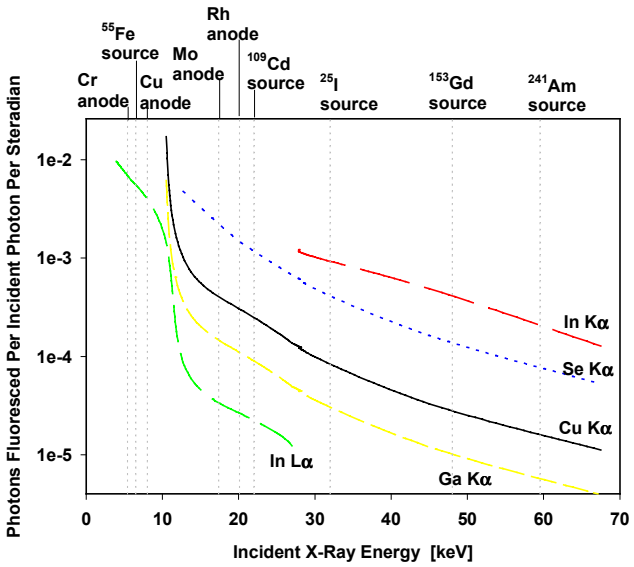

Figure 1: Calculated primary fluorescence sample yield for a 2.5 μm CIGS sample as a function of incident x-ray energy.

2.2.a High-Resolution XRF Measurements

Initial XRF measurements were made at Lockheed Martin Astronautics (LMA). The LMA XRF system consists of a 30 keV, 3 mA x-ray tube with Rh anode, source and detector collimators, and a liquid nitrogen-cooled Si(Li) detector. The system components were obtained by dissambling an outdated XRF measurement station previously sold by Kevex Instruments. Figure 2 shows a spectrum taken using the LMA XRF system. The x-axis is fluoresced x-ray energy, and the y-axis is number of counts. The arrows in the figure highlight the 240 eV full width at half maximum on the Cu Kα emission.

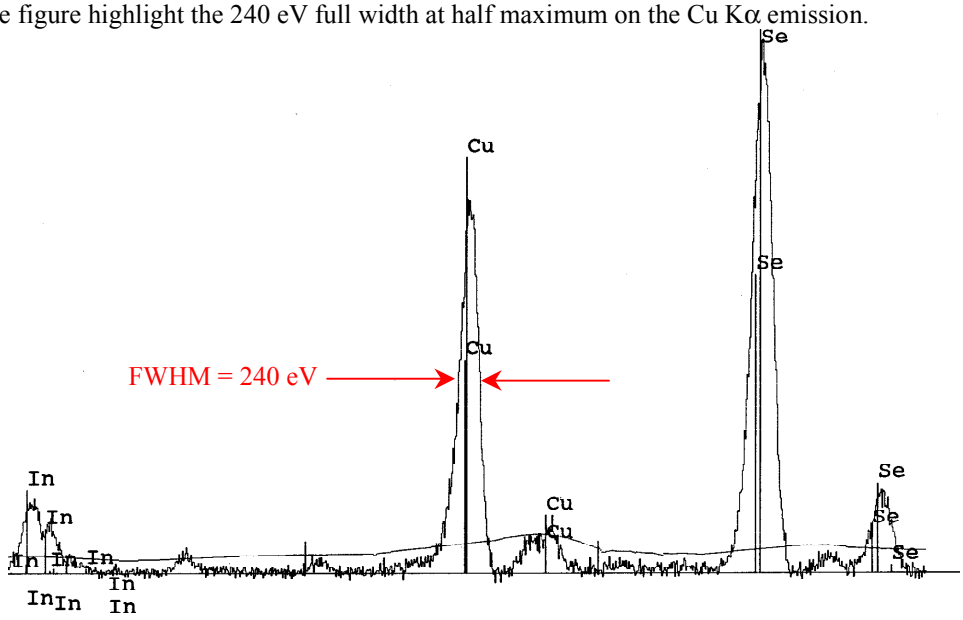

Figure 2: Spectrum of CIS sample taken at LMA.

A number of difficulties were encountered with the LMA XRF system. First, the system was found to be contaminated with Cu, i.e. significant Cu emission was seen even when measuring high-purity

samples containing no Cu. Second, signal analysis was performed by proprietary Kevex routines, and Kevex personnel would not divulge the details of these routines. Furthermore, the Kevex software does not allow data access to third party applications, such as those performing deposition chamber control. Third, the source and detector on the LMA system are not commercially available. Replication of the source and detector with similar models that are currently commercially available was found to cost in excess of $150,000.

2.2.b Low-Cost, Commercially-Available XRF

To resolve the difficulties experienced with the LMA XRF system, a low-cost, commercially available system was assembled at MRG. X-rays are supplied by a 50 W Oxford XTF5016 x-ray tube with Rh anode, operated at 40 kV and 250 μA. X-rays are detected by an Amptek XR100CR 7mm Si PIN photodiode. Data acquisition is controlled by custom Visual Basic software through use of an EG&G Trump 2K multi-channel buffer board. Analysis is performed by the custom software, and all data quantities are accessible to third-party software, such as that used to control the deposition chamber. Total parts cost for this system is about $30,000. Figure 3 shows a schematic diagram and a photograph of the low-cost sensor, in the configuration used for ex-situ development of analysis and hardware.

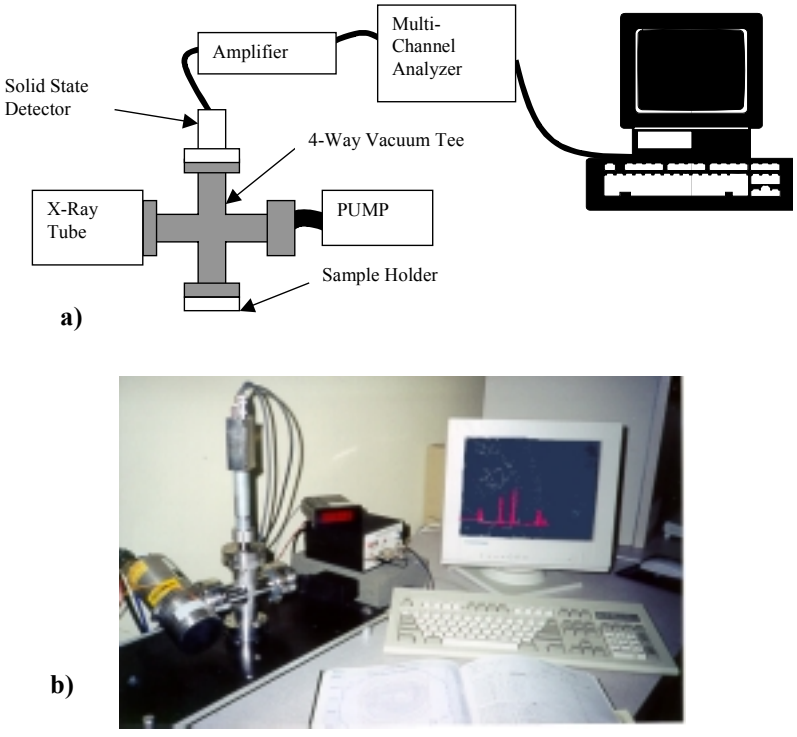

Figure 3: a) Schematic diagram and b) photograph of low-cost XRF sensor used for ex-situ development.

One challenge of using lower-cost components is the lower resolution of the x-ray spectra, and therefore increased difficulty in separating the emission of various elements. Figure 4 shows the x-ray spectrum of a typical CIGS sample on a steel substrate. The relevant emission peaks are labeled. The arrow in the figure highlights the 340 eV full width at half maximum of the Cu Kα emission. At this resolution, the Cu Kβ and the Ga Kα emission peaks overlap. The method developed for mathematically separating these two peaks is discussed in section "2.3 Analysis Method".

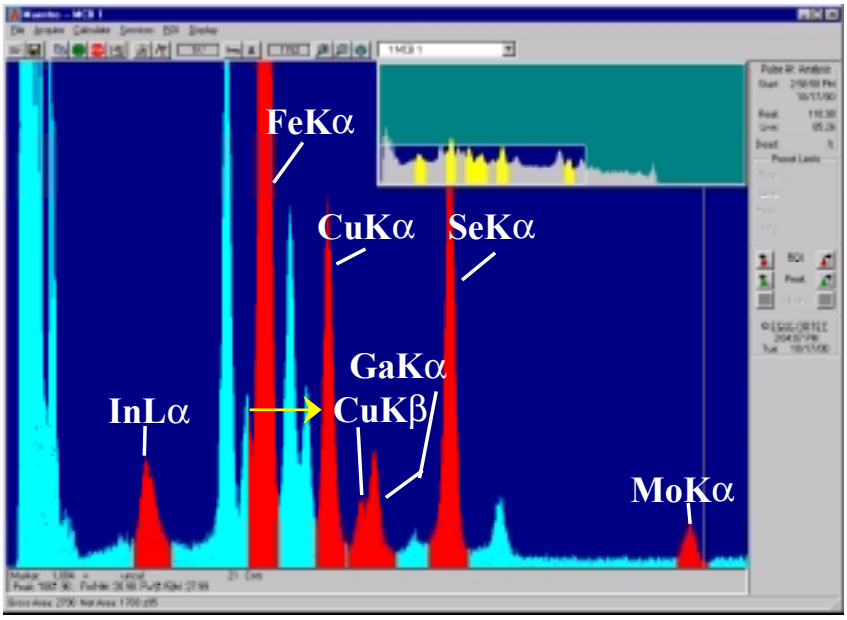

Figure 4: XRF spectrum of CIGS on steel, using low-cost sensor.

2.3 Analysis Method

Qualitative interpretation of XRF signals is simple: the more of a given element is present, the stronger is that element's fluorescence. Quantitative interpretation, however, becomes more complicated, since interactions occur between the signal from one element and the other elements in the sample. These interactions occur in two manners: absorption of incident and fluoresced x-rays by the other elements, and excitation of the given element by x-rays fluoresced from the other elements ("secondary fluorescence"). Thus, a number of numerical methods, ranging from fully empirical to those based on fundamental parameters, exist for extracting sample composition from XRF signals.[3,4,5,6,7,8,9,10] Important requirements for such a method to be used on CIGS samples are the ability to interpret signals from multi-layer samples, to account for variations in substrate and back contact thickness, to interpret signals from samples with varying Ga gradients, to calculate compositions and thicknesses quickly in real-time, and to handle samples with intermediate film thicknesses where neither thick-film or thin-film approximations are valid. The approach to be taken is similar to that used by de Jongh for analysis of stainless steels[10]. The relationship between the composition of the sample and the XRF counts is expressed as a first-order Taylor expansion, and the coefficients in the Taylor expansion are calculated numerically from first principles prior to run-time. These first-order relationships are then algebraically inverted to extract the parameters describing the physical make-up of the CIGS sample.

2.3.a Simulation Tool

Simulation from first principles is used to calculate the Taylor expansion coefficients described in the preceding paragraph. The simulation tool software developed to perform such calculations is also useful for answering questions about expected magnitudes of various effects on analysis, such as gradients or varying back contact thickness. This section describes the theoretical basis for and the implementation of the simulation tool.

The equations that predict magnitude of x-ray fluorescence signals from a homogeneous, single-layer sample are well known, although complicated[11]. This analysis was extended to multi-layer samples at MRG, to find the fluorescence from a multi-layer sample. It was deduced that the photons per area, per solid angle, detected from the fluorescence of element i in layer k is

$$P_{i,k} = q\ E_{i,k}\ C_{i,k}\ e^{-\frac{1}{\sin \Psi_2}\sum_{\ell=1}^{k-1} \mu_{s\ell}(\lambda_{i,k})\,\rho_\ell\, h_\ell} \bullet$$
$$\int_{\lambda_o}^{\lambda_{abs,i,k}} \left\{1 - e^{-\rho_k\ h_k\left(\frac{\mu_{sk}(\lambda)}{\sin\psi_1} + \frac{\mu_{sk}(\lambda_{i,k})}{\sin\psi_2}\right)}\right\} \bullet$$
$$e^{-\frac{1}{\sin\psi_1}\left[\sum_{\ell=1}^{k-1} \mu_{s\ell}(\lambda)\rho_\ell h_\ell\right]} \quad \frac{\mu_{ik}(\lambda)\mathrm{I}_\circ(\lambda)\,d\lambda}{\mu_{sk}(\lambda) + \frac{\sin\psi_1}{\sin\psi_2}\mu_{s,k}(\lambda_{i,k})}$$

(1)

where

$P_{i,k}$ = the photons per second per area of illuminated sample fluoresced into the specified solid angle
k = index specifying which layer in the sample
i = index specifying which element within layer k
ℓ = index used for sums over multiple layers
Ψ_1 = the angle between the incident x-ray beam and the sample surface
Ψ_2 = the angle between the sample surface and the path from the illuminated spot to the detector
q = the geometric factor $\frac{\sin\psi_1}{\sin\psi_2}\frac{d\Omega}{4\pi}$, where dΩ is the solid angle subtended by the detector, relative to the sample
$E_{i,k}$ = the excitation factor, which involves the quantum mechanical probability of the photons of interest being produced and escaping the atom
$C_{i,k}$ = the concentration by weight of element i in layer k
$\lambda_{abs,\,i,\,k}$ = absorption edge wavelength of element i in layer k
λ_0 = the highest energy wavelength present in the incident x-rays
λ = the variable used to integrate over all the wavelength range of the incident x-rays
$\lambda_{i,k}$ = the fluorescence wavelength of element i in layer k
$\mu_{s\ell}$ = the mass absorption coefficient of the layer ℓ
μ_{sk} = the mass absorption coefficient of the layer k
μ_{ik} = the mass absorption coefficient of element i in layer k
ρ_ℓ = the density of layer ℓ
ρ_k = the density of layer k
h_ℓ = the thickness of layer ℓ
h_k = the thickness of layer k
I_0 = number of incident photons per second per area at a given wavelength

The secondary fluorescence, i.e. fluorescence excited not from the incident x-rays but from a constituent element's fluorescence, can also be calculated. At MRG, the standard secondary fluorescence expression was expanded to include multiple layers. It was found that the number of photons per solid angle detected due to the secondary fluorescence of element i in layer k excited by element j in layer ℓ is

$$S_{i,j,k,\ell} = \frac{1}{2} qE_i C_{ik} E_j C_{j\ell} \frac{\rho_k \rho_\ell}{\sin\psi_1} \mu_i(\lambda_j) \int_{x_\ell=0}^{t_\ell} \int_{y_k=0}^{t_k} U'(x_\ell, y_k)\, A'(x_\ell)\, B'(y_k)\, dx\, dy$$

(2)

where

$$U'(x,y) = \int_{\alpha=0}^{90^{\circ}} \tan(\alpha)\ \xi\ d\alpha$$

$$A'(x_\ell) = \int_{\lambda_{\min}}^{\lambda_{abs,j}} \mu_j(\lambda_{inc})\, I_\lambda\, A_1 \exp\left[\frac{-1}{\sin\psi_1}\left(\mu_{s\ell}(\lambda_{inc})\rho_\ell x_\ell + \sum_{p=1}^{\ell-1}\mu_{sp}(\lambda_{inc})\rho_p t_p\right)\right] d\lambda_{inc}$$

$$B'(y_k) = \exp\left[-\mu_{sk}(\lambda_i)\rho_k \frac{y_k}{\sin\Psi_2} - \sum_{p=1}^{k-1}\mu_{sp}(\lambda_i)\rho_p \frac{t_p}{\sin\psi_2}\right]$$

$$\xi = \begin{cases} \exp\left[-\mu_k(\lambda_j)\rho_k \dfrac{|x-y|}{\cos\alpha}\right] & (\ell = k) \\ \exp\left[-\sum_m \mu_m(\lambda_j)\rho_m \dfrac{t_m}{\cos\alpha} - \mu_\ell(\lambda_j)\rho_\ell \dfrac{x_\ell}{\cos\alpha} - \mu_k(\lambda_j)\rho_k \dfrac{(t_k - y)}{\cos\alpha}\right] & (\ell > k) \\ \exp\left[-\sum_m \mu_m(\lambda_j)\rho_m \dfrac{t_m}{\cos\alpha} - \mu_\ell(\lambda_j)\rho_\ell \dfrac{(t_\ell - x)}{\cos\alpha} - \mu_k(\lambda_j)\rho_k \dfrac{y}{\cos\alpha}\right] & (\ell < k) \end{cases}$$

α = Variable of integration in $U'(x,y)$
A_1=incident beam area
and other variables are as defined in equation (1).

The integrals in equations (1) and (2) are calculated numerically by the simulation tool. Algorithms are included to insure that the error introduced by the finite step size in the numerical integration stays below the specified maximum percent error. Incident spectra and fundamental constants such as densities and mass absorption coefficients are taken from the literature[12]. The simulation tool outputs the magnitude of primary and secondary fluorescence emission lines from multi-layer samples, where each layer contains multiple elements. Emission from both K and L transitions is calculated.

A number of tests have been performed to verify the simulation output. Comparisons of the simulator output both with simplified theoretical expressions and with published data have been made.

One such test involves comparing the simulation tool output with simplified fluorescence expressions. For very thick and very thin films, equation (1) can be simplified considerably[13]. In such cases, for monochromatic incident x-rays, the integral in equation (1) can be performed, and algebraic expressions for the primary fluorescence can then be written. Figure 5 shows the simplified theoretical expressions for the fluorescence from thick and thin Cu films, shown as the solid and dotted lines, respectively. The simulator output is also shown, and agrees with the theoretical expressions over the appropriate thickness ranges. As expected, for very thick films the count rate is independent of the film thickness. The count rates shown on the y-axis are for a specified system geometry and incident x-ray flux, and therefore should not be taken as a general indicator of count rates.

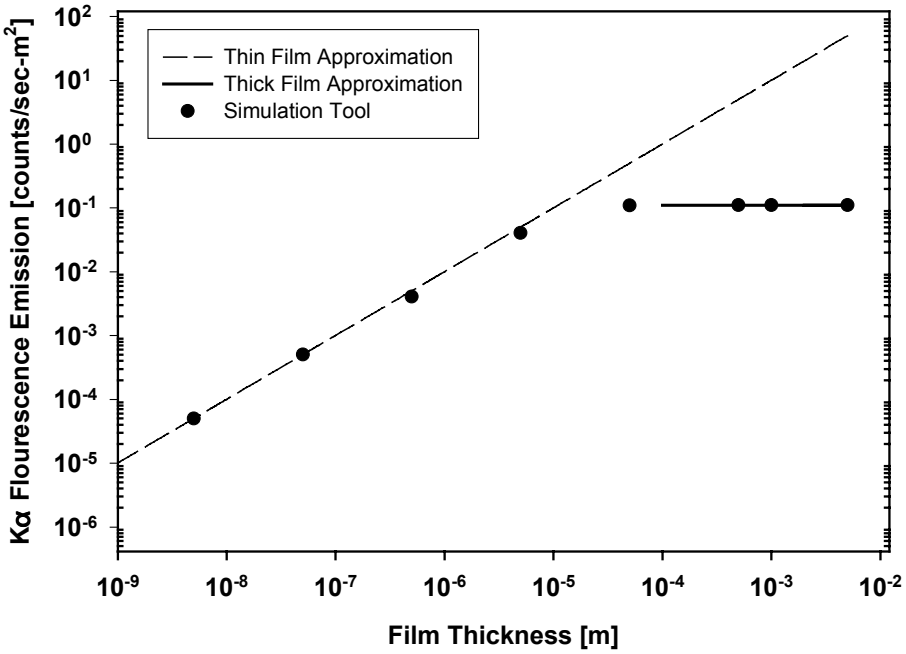

Figure 5: Comparison of simulator output with theoretical expressions for Kα primary fluorescence of thick and thin Cu films.

Similarly, a simplified expression for the secondary fluorescence of thick films can also be obtained[14]. Simulator output was shown to agree with the simplified theoretical expression for secondary fluorescence as well.

Simulation output was tested against published XRF data. For example, Bush and Stebel[15] measured the XRF of Ag films of varying thickness on Cu substrates. The change in Ag signal and Cu signal they measured is plotted in Figure 6 as the filled points. The output of the XRF simulator is shown as the open points, and agrees well with the measured data.

Simulation output for secondary fluorescence was also tested against published XRF data. For example, Pollai et al.[16] calculated the ratio of secondary to primary fluorescence intensity as a function of film thickness for Cu-Co alloys. MRG simulator output was compared with the published data, as shown in Figure 7. The filled circles show Pollai's data. The open squares show the simulator output, which agrees well with Pollai's data. It should be noted that the ratio of secondary to primary fluorescence depends strongly on the incident x-ray spectrum. The gray triangles show the simulator output when Rh characteristic radiation is used as the incident spectrum, rather than the typical Rh tube spectrum that includes continuous as well as characteristic radiation.

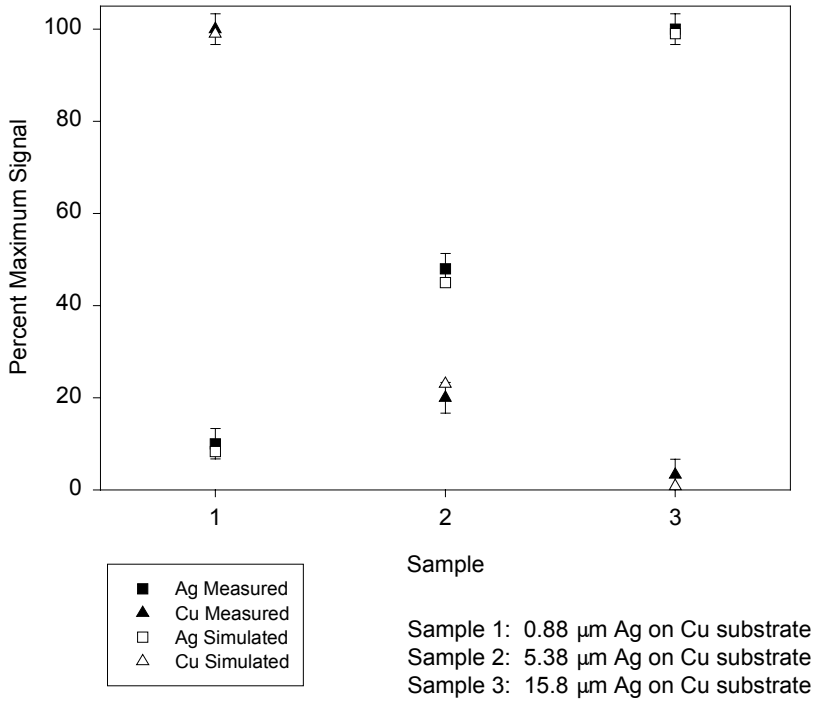

Figure 6: Measured and calculated change in Ag and Cu XRF signals for Ag layers of varying thicknesses on Cu substrates.

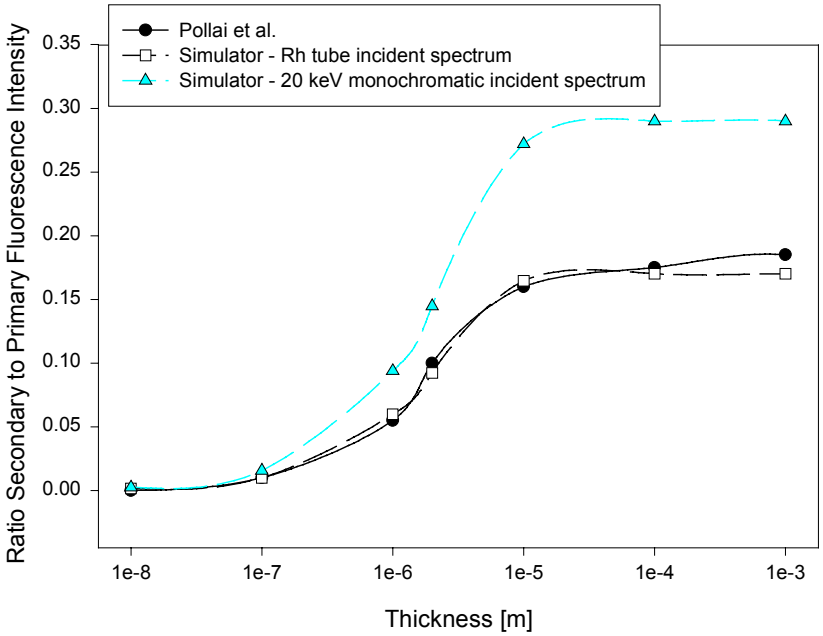

Figure 7: Ratio of secondary to primary fluorescence intensity versus film thickness for 50% Cu - 50% Co alloys.

2.3.b Analysis Steps

Conversion of x-ray emission to composition is based on pre-calculation of expected emissions, requiring only one CIGS calibration sample. Before measurement, a one-time mapping of expected emissions over a broad range of compositions is performed and stored to disk using the simulation tool described in section "2.3.a Simulation Tool". This one-time mapping is specific to the incident x-ray angle, incident x-ray energy, and the fluoresced x-ray angle. Then, a single calibration sample of known composition is used to account for geometric factors and detector efficiency. The calibration sample essentially establishes the factors of proportionality relating the measured counts to the pre-calculated counts. The calibration sample information is stored in a file and is loaded automatically upon starting the measurement software.

During measurement, software identifies the pre-mapped, calculated, emission point that most closely matches the emission of test sample. Then, the software performs a first-order expansion about this emission point. The differences between the test sample emission and the pre-mapped emission are used to invert the first-order expansion and solve for the test sample composition. The equations used to solve for the test sample composition are:

$$\begin{aligned}
\Delta C_{InL\alpha} &= \Delta t_{In}\frac{dC_{InL\alpha}}{dt_{In}} + \Delta t_{Cu}\frac{dC_{InL\alpha}}{dt_{Cu}} + \Delta t_{Ga}\frac{dC_{InL\alpha}}{dt_{Ga}} + \Delta t_{Se}\frac{dC_{InL\alpha}}{dt_{Se}} \\
\Delta C_{CuK\alpha} &= \Delta t_{In}\frac{dC_{CuK\alpha}}{dt_{In}} + \Delta t_{Cu}\frac{dC_{CuK\alpha}}{dt_{Cu}} + \Delta t_{Ga}\frac{dC_{CuK\alpha}}{dt_{Ga}} + \Delta t_{Se}\frac{dC_{CuK\alpha}}{dt_{Se}} \\
\Delta C_{GaK\alpha} &= \Delta t_{In}\frac{dC_{GaK\alpha}}{dt_{In}} + \Delta t_{Cu}\frac{dC_{GaK\alpha}}{dt_{Cu}} + \Delta t_{Ga}\frac{dC_{GaK\alpha}}{dt_{Ga}} + \Delta t_{Se}\frac{dC_{GaK\alpha}}{dt_{Se}} \\
\Delta C_{SeK\alpha} &= \Delta t_{In}\frac{dC_{SeK\alpha}}{dt_{In}} + \Delta t_{Cu}\frac{dC_{SeK\alpha}}{dt_{Cu}} + \Delta t_{Ga}\frac{dC_{SeK\alpha}}{dt_{Ga}} + \Delta t_{Se}\frac{dC_{SeK\alpha}}{dt_{Se}}
\end{aligned} \qquad (3)$$

where

ΔC_i = for emission peak i, the difference in counts between the calculated emission point and the measured test sample

Δt_k = for element k, the difference in thickness between the calculated emission point and the test sample. This is the desired result of the measurement

$\frac{dC_i}{dt_k}$ = the calculated change in the counts from emission peak i for a change in the thickness of element k, evaluated at the calculated emission point

For a given measurement, the Δt_k's are the only unknown quantities in these equations. Finding the sample composition is therefore simply just a matter of solving algebraic equations for the Δt_k's.

The equations above require emission measurements from the InLα, CuKα, GaKα, and SeKα peaks. The InLα, CuKα, and SeKα peaks are well-resolved and separate from Mo and Fe emissions. As can be seen in Figure 4, however, the GaKα peak overlaps with the CuKβ peak. From first principles, the magnitude of the CuKβ emission is related to that of the CuKα emission by a constant factor. Also, the slightly different absorption of the Cu Kα and Kβ radiation in the sample (due to the differing emission energies) can be calculated and compensated for. Thus, through a measurement of the CuKα emission, the CuKβ emission can be calculated and subtracted from the GaKα region of interest counts, resulting in an accurate determination of the actual GaKα emission.

Several refinements can be made to the thickness calculation, as chosen by the operator. The magnitude of the substrate (or back contact) signal can be used to correct for fluctuations in tube intensity or variations in the sensor-to-sample distance. The varying absorption of the test samples – based on its composition and thickness - is accounted for when performing the normalization of the signal to the correct Mo or substrate signal intensity. An additional refinement can be performed for background counts due to substrate emission. Typical bare soda-lime glass emits as much fluorescence in the InLα region of interest as over 5000 Å of In. However, because the InLα emission is at relatively low x-ray energy, such x-rays are easily absorbed. The background contribution of the glass to the sample measurement is therefore strongly dependent on the back contact and CIGS thickness. The operator can choose to account for the dependency of background counts on back contact and CIGS thickness for glass substrates. Each refinement described above require an iterative calculation, since the refinement both depends on and affects the results of the thickness calculations. Finally, if test samples are expected to be similar to the calibration sample, a significant fraction of the calculation time can be removed by assuming that the pre-mapped point corresponding to the calibration sample will always be the point used for the first-order expansion.

2.4 Ex-Situ Measurements and Results

Calculation techniques were developed and tested with ex-situ measurements before in-situ tests were performed. The compositions extracted from XRF measurements have shown good agreement with inductively coupled plasma (ICP) measurements over a large variety of samples. An example of results of ex-situ XRF measurements, made using the in-situ components, are shown in Figure 8. The x-axis shows the ratio Cu/(In+Ga) as measured by ICP at the National Renewable Energy Laboratory (NREL). The y-axis shows Cu/(In+Ga) as measured by XRF. Error bars in the x-direction represent uncertainty in the ICP measurement, whereas error bars in the y-direction reflect noise in the XRF measurement and error due to sample nonuniformity. The range of compositions represented Figure 8 span high-efficiency CIGS samples by an appreciable percent. High efficiency CIGS devices typically contain about 3100 Å Cu, 5200 Å In, 1300 Å Ga, and 15000 Å Se. Cu thicknesses in the samples of Figure 8 range from 500 to 3600 Å, In thicknesses range from 600 to 16000 Å, Ga thicknesses range from 0 to 8400 Å, Se thicknesses range from 8100 to 31000 Å, and Mo thickness range from 2500 to 110000 Å. (In this report, the amount of each element is quoted in terms of effective thickness. Thicknesses are deemed "effective" because the XRF actually measures the number of atoms present. For more intuitive reporting, atoms per sample area has been converted to effective thickness by use of the elemental density and atomic weight.) The samples of Figure 8 were deposited on soda lime glass, lightweight aerospace glass, and polyimide.

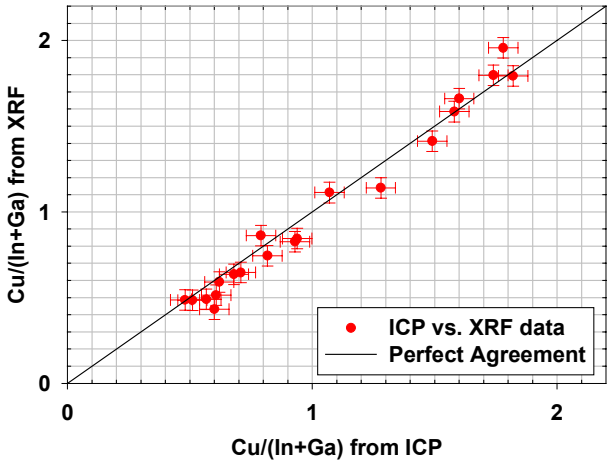

Figure 8: Atomic ratio Cu/(In+Ga) as measured ex-situ by XRF and ICP.

Good agreement is also seen between ICP and the XRF analysis for the ratio Ga/(In+Ga). For the samples of the previous graph that contained Ga, the atomic ratio Ga/(In+Ga) is shown in Figure 9.

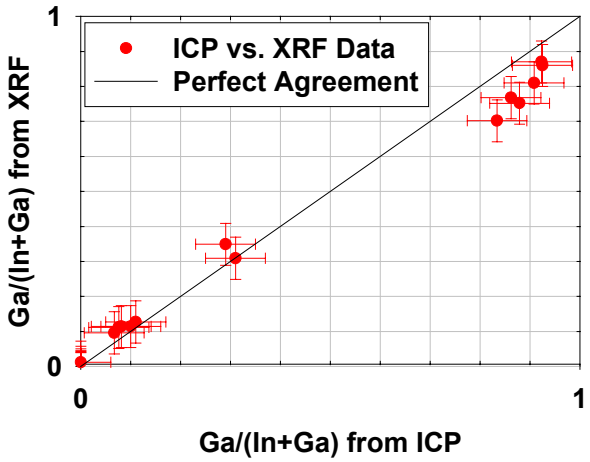

Figure 9: Atomic ratio Ga/(In+Ga) as measured ex-situ by XRF and ICP.

3. In-Situ XRF

In-situ XRF sensors were installed on CIGS production roll-coaters at GSE. The first sensor was installed in June, 2000. A second sensor, with a slightly improved design, was installed on a second roll-coater at GSE in November, 2000. Figure 10 shows photographs of these sensors. Plans to install further XRF sensors are in place. This section describes the hardware necessary to adapt the XRF measurements to the in-situ environment, and shows real-time data acquired during CIGS depositions.

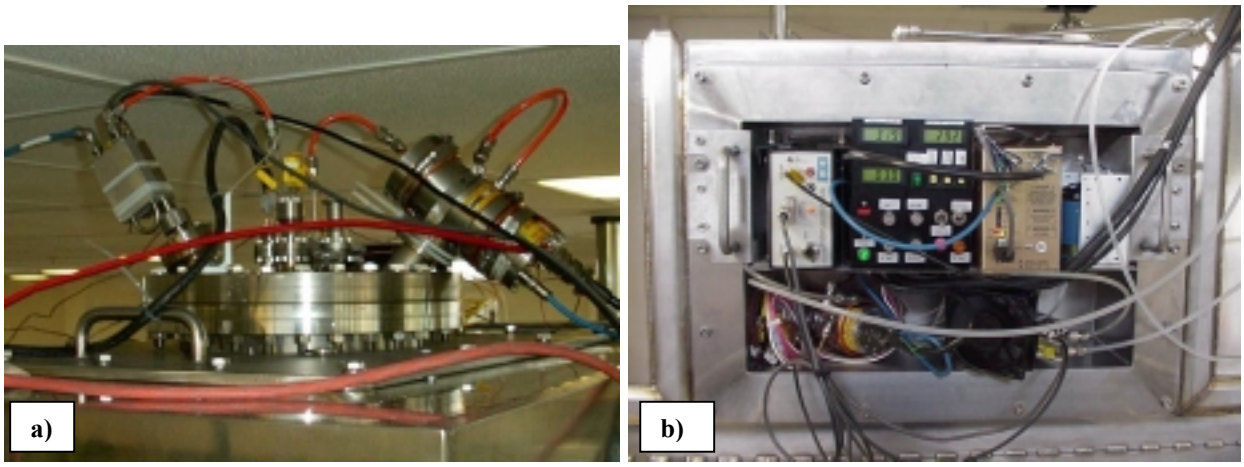

Figure 10: a) First and b) second in-situ XRF sensors installed at GSE.

3.1 In-Situ Hardware

Installation of XRF equipment in the CIGS deposition environment requires protection of the sensor from Se exposure and elevated temperatures. Protection of the x-ray source and detector from Se exposure is achieved by use of thin polyimide barriers that block Se but transmit x-rays. Figure 11 shows the fluorescence spectrum of a CIS sample with and without polyimide barriers installed. At all but the lowest

energies, the absorption of the barriers is negligible, and even at the lowest energies the transmitted signal is appreciable. These barriers are heated to 200 ^{o}C to drive off Se. Sensor parts are cooled. They are shielded from Se by baffles that force any Se atom travelling toward the sensor to undergo multiple collisions with cooled surfaces. The design of the Se protection is shown in Figure 12. The figure is drawn according the first XRF sensor installed at GSE (Figure 10a), but the basic design is the same for each. A 13.25" ConFlat (CF) plate is machined and welded to accommodate the appropriate feedthroughs for the source and detector. Smaller feedthroughs at the center of the plate accommodate the necessary cooling, power, and temperature measurement. The machined plate and fittings are cross-hatched in Figure 12.

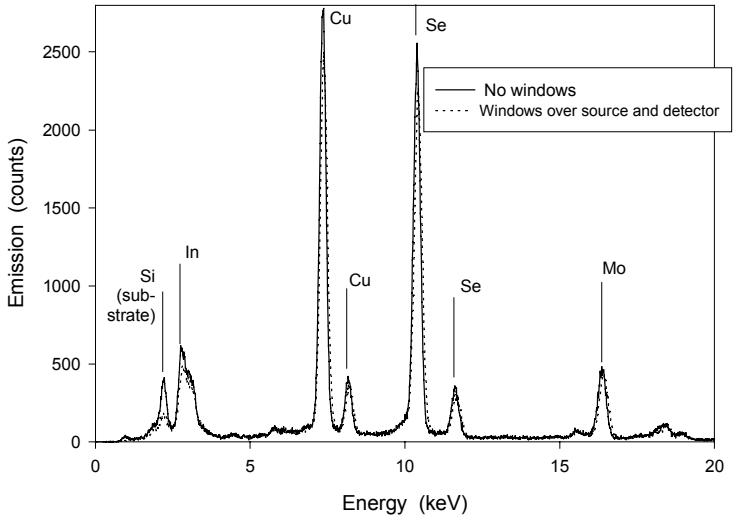

Figure 11: Fluorescence spectra of CIS sample with and without polymer barriers installed.

Figure 12 a) shows the cooled inner envelope of the Se protection. A Cu sleeve (shown as dotted) is press fit into each of the two thin flanges on the welded plate. Hidden (dotted) lines indicate the portions of the Cu tubes that extend into the large diameter tubes on the welded plate. Water cooling lines are shown as shaded. On the source side, the Cu sleeve blocks the straight path of the Se to the x-ray source from venting holes on the side of the large diameter tube. On the detector side, the Cu tube both blocks Se flow and cools the x-ray detector. The x-ray detector inserts into the Cu tube so that it is about 0.5" from the tube end. Aperture pieces are inserted into the tips of each Cu tube. Such aperture pieces insure that the x-ray source illuminates only the desired sample area, and that the detector looks only at the desired sample area, not secondary fluorescence from other parts of the chamber.

Figure 12 b) shows the heated outer envelope of the Se protection. The outer envelopes are made of multiple 2 ¾" CF flanges. Each CF flange is separated by a polymer gasket, a Cu gasket, and another polymer gasket. The gaskets are *not* included to provide a better seal between the flanges. Rather, the gaskets minimize the contact area, and therefore the heat flow, between neighboring flanges. The outer polyimide window, to block Se flow, is inserted underneath the last flange in each stack (i.e. the flange closest to the CIGS). A heater band is wrapped around the last flange on each stack. Small vent holes are drilled in the large diameter tubes, near the cooling lines, so that the polyimide windows do not need to withstand large pressure differentials when pumping and venting. The sensor electronics are those in the ex-situ system, as described in section "2.2.b Low-Cost, Commercially-Available XRF".

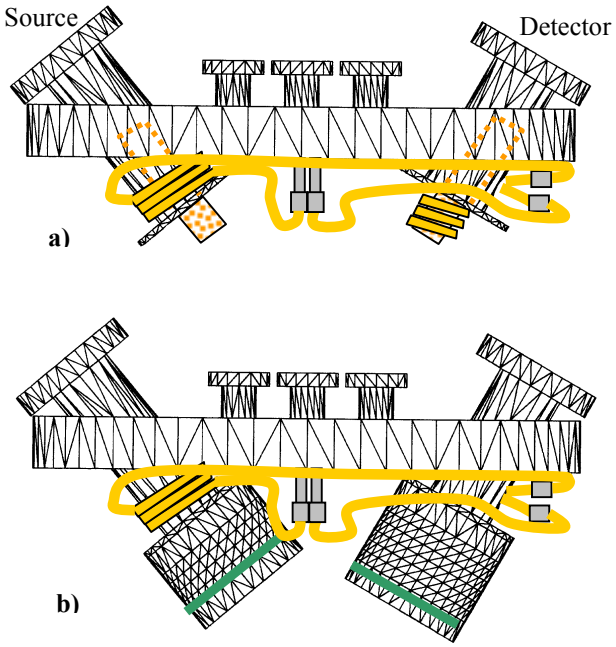

Figure 12: Design of the Se protection hardware. a) The cooled inner envelope and b) the heated outer envelope are shown.

3.2 In-Situ Results

Film composition and thickness are currently being monitored in-situ by XRF at GSE. Film composition and thickness are measured after the deposition by electron-activated energy dispersive spectroscopy (EDS) and scanning electron micrograph (SEM) cross-section at GSE.

The XRF and EDS / SEM measurements indicate comparable values for total film thickness, Cu/(In+Ga), Cu thickness, and Se thickness. For example, Figure 13 shows total film thickness as a function of position along a 50-ft. test run. The filled circles show SEM data, and the +'s show XRF data. Similarly, Figure 14 compares the ratio Cu/(In+Ga) as measured by XRF with that measured by EDS. Agreement is best for values of Cu/(In+Ga) near that of the calibration sample (0.85). It is possible that as the film becomes In-rich, phase segregation occurs within the film, creating a nonuniform compositional profile. EDS is very sensitive to compositional profiles, whereas XRF is not.

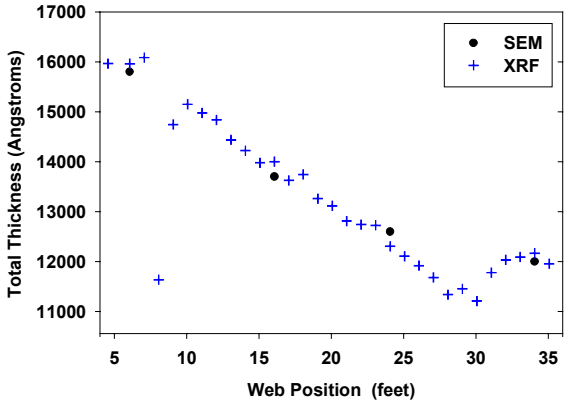

Figure 13: Total film thickness as measured by EDS and XRF.

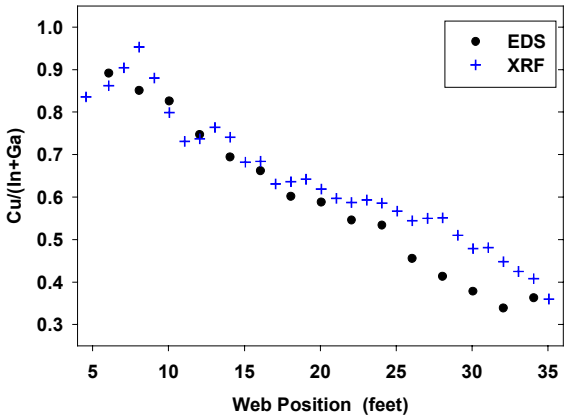

Figure 14: Atomic ratio Cu/(In+Ga) as measured by EDS and XRF.

An offset exists between EDS and XRF results for In and Ga thicknesses. Compared to the EDS, the XRF consistently overmeasures the In thickness, and undermeasures the Ga thickness. The ratio Ga/(In+Ga) is therefore undermeasured by the XRF, as compared to the EDS. This relationship is shown in Figure 15.

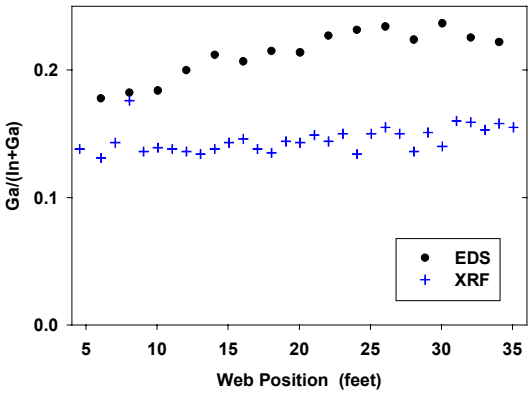

Figure 15: Atomic ratio Ga/(In+Ga) as measured by EDS and XRF.

Ga profiling may be the root of the disagreement between the XRF and EDS. The XRF measurement is an indicator of average film composition. Calculations indicate that locating all the Ga at the back of the film, as opposed to evenly distributing it throughout the film, causes only a ~10% difference in the measured Ga XRF signal. EDS, on the other hand, does not see the back of the film. The measured composition is a weighted average extending about 1 micron into the film. In addition to ex-situ tests of Ga/(In+Ga) (as shown in Figure 9), initial ICP measurements on the test run of the previous three figures have confirmed that XRF measurements indicate changes in the bulk composition more closely than EDS measurements, as shown in Figure 16. ICP measurements were made at the National Renewable Energy for three locations in the test run, as well as for the sample used to calibrate the XRF sensor. In Figure 16, the Ga content of various positions on the test run is plotted as the fraction of that contained in the calibration sample.

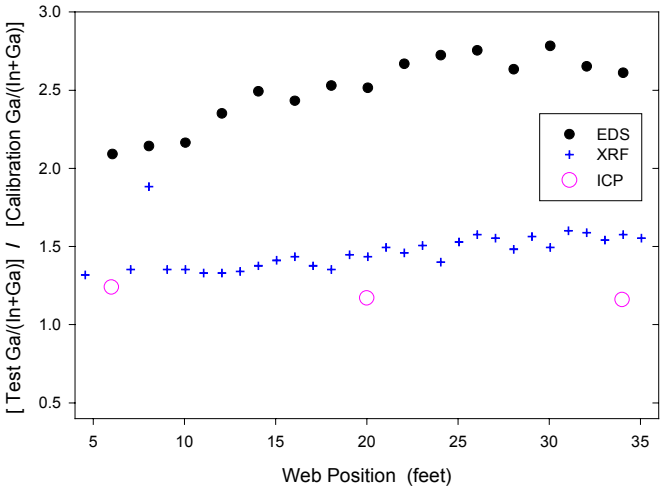

Figure 16: Change in Ga/(In+Ga) in moving from calibration sample to test sample, as measured by EDS, XRF, and ICP.

The first XRF sensor installed at GSE has been exposed to over 600 hours of CIGS deposition to date, not including system heat-up and cool-down times. No evidence of Se contamination of the source or detector is yet apparent. The comparison between EDS and XRF measurements also appears to be stable, as long as sensor settings are not changed.

3.3 Noise Limitations

The accuracy of the XRF measurement is improved when signal-to-noise ratio is improved, and when signal magnitude (signal counts per measurement) is improved.

The largest source of noise when measuring CIGS on steel substrates is the large number of background counts from the substrate. (This source of noise is negligible when measuring CIGS on glass or polyimide.) Thus, signal-to-noise ratio can be improved by improving the ratio of counts from the CIGS to those from the steel. Thicker CIGS, thicker back contact layer, or smaller x-ray angle of incidence will increase the signal-to-noise ratio.

In general, signal magnitude can be increased by decreasing distance from the source or detector to the sample, increasing illuminated spot size, increasing tube output, or increasing measurement time. The first three methods listed increase count rate, and therefore cannot be used for steel substrates, since the high count rate from the substrate saturates the detector and destroys the signal resolution. Figure 17 shows how increased measurement time can increase accuracy. Cu thickness is graphed as derived from repeated measurements on a single CIGS on steel sample using exposure times of 1 minute (filled circles), 2 minutes (open circles), and 3 minutes (triangles). Statistical information is also listed in the figure. As the measurement time increases, the standard deviation σ and minimum-to-maximum variation decrease. Uncertainty in standard deviation based on 90% confidence intervals is shown as $\Delta\sigma$. The data of Figure 17 represent worst case conditions for signal-to-noise. The sample is thin (1.5 µm total thickness for CIGS and Mo back contact), x-rays were incident at a fairly high angle (50^{o}), and the sample substrate is steel.

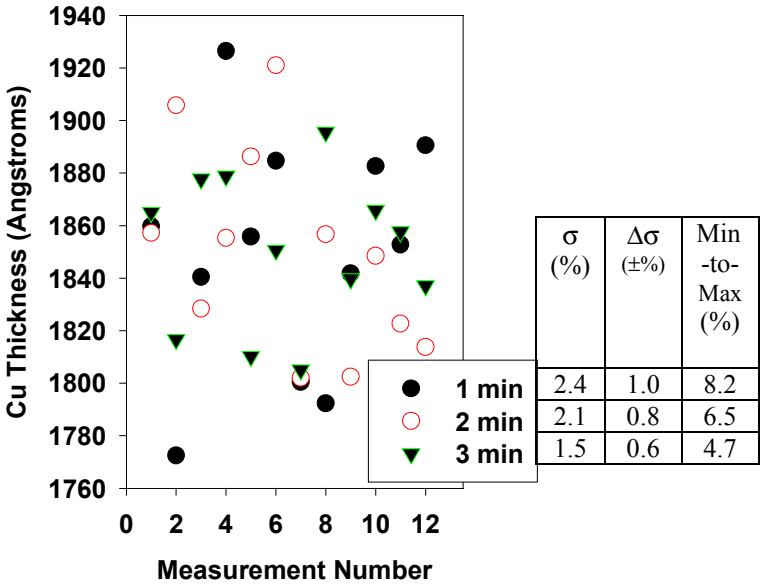

σ (%)	Δσ (±%)	Min -to- Max (%)
2.4	1.0	8.2
2.1	0.8	6.5
1.5	0.6	4.7

Figure 17: Repeated XRF measurements of Cu thickness on the same sample for a variety of exposure times.

Improvements in signal-to-noise ratio were achieved from the first to the second in-situ XRF sensor installed at GSE. A 20% increase in the ratio of film emission to substrate emission was achieved by using a shallower angle of incidence for the exciting x-rays. A 51° angle of incidence was used in the first sensor. This angle was decreased to 41° for the second sensor. The main constraint keeping one from decreasing the angle of incidence further is the increasing width of the chamber wall area required for the sensor feedthroughs.

3.4 Comparison of XRF with Other In-Situ Sensors

The in-situ XRF sensor brings a unique set of capabilities and requirements to the group of sensors that may be useful during CIGS deposition. First, XRF measures film properties – the amounts of each element deposited – rather than deposition rates. To measure deposition rates, various groups have used atomic absorption (AA), quartz crystal microbalances (QCM), and electron impact emission spectroscopy (EIES). Second, fluorescence from the sample is largely independent of direction. This isotropic emission has both advantages and disadvantages for in-situ sensing. It implies that precise alignment of the sample to the sensor is unneccessary. Slight variations in sample-to-sensor distance - or in x-ray tube current - have little effect on interpretation and can be corrected for using the substrate signal. In contrast, techniques based on reflection (R) - including ellipsometry[17] - require precise alignment of optical source, sample, and detector. The isotropic emission also implies, however, that intensity decreases with the square of the distance to the sample, yielding a $\sim 1/r^4$ overall dependence of signal on sensor-to-sample distance, when the fall-off in intensity from the x-ray source is included. This rapid decrease in signal with distance makes a substantial challenge of locating XRF in the CIGS deposition zone, where significant removal of the sensor from the substrate may be required to avoid blocking deposition flux and to avoid thermal loads. The comparisons made above are summarized in Table 1. The last line in Table 1 also compares approximate sensor costs. XRF cost is the total expenditure for the parts needed to assemble the sensor described in this report. AA, QCM, and EIES costs are that of typical units as might be purchased from commercial distributors. R cost is based on expenditure for parts to perform visible spectroscopic ellipsometry. Because measurement time and accuracy for each sensor are highly dependent on deposition rates and system configuration, they are not compared here.

	XRF	AA	QCM	EIES	R
Measures:	Film properties	Rates	Rate	Rates	Film Properties
Multiple Elements	Yes	Yes, but not Se	No	Yes, but not Se	Yes
Morphology	No	No	No	No	Yes
Alignment	Somewhat important	Important	Important	Important	Critical
In Deposition Zone	Not with current design	Yes	Very Close	Very Close	Yes
Cost (k$)	25	45	5	40	50

Table 1: Comparison of qualities of five CIGS deposition sensors.

4. Applicability of XRF to other layers in PV

The applicability of in-situ XRF to other layers in the CIGS module is determined by several factors. First, the sensor must be operational in that layer's deposition environment. Second, the elements of interest must be visible in the fluorescence spectrum. They must have fluorescence energies above the systems low-energy detection limit and excitation energies below the incident x-ray energy. Being visible in the fluorescence spectrum also requires that they be resolved from primary emissions of other elements in the same layer or in previously deposited layers. Third, enough accuracy in composition or thickness must be obtained so that the important film properties are controlled. Finally, the information gained must merit the cost of the sensor, particularly when other sensors may be available for obtaining the same information.

The layers considered for XRF control are Mo, CIGS, CdS, ZnO (both conductive and insulating), and ITO. The energies of the Kα and Lα emissions of the constituent elements are shown in Figure 18. Each emission peak is labeled. The emissions are shown with a 340 eV full width at half maximum, typical of the current in-situ hardware. The dashed vertical line is the characteristic emission energy of the current x-ray source.

Thickness and composition of the first two layers of the CIGS devices, Mo and CIGS, can be measured using the current in-situ XRF sensor. As seen in Figure 18, the peaks from Mo Kα, Cu Kα, In Lα, Ga Kα, Se Kα are well-separated and can be excited by the x-ray tube primary emission. However, because Mo is a single-element deposition, Mo deposition is expected to be well-suited for quartz crystal microbalance rate monitoring. It is therefore unclear whether the expense of XRF merits its use for Mo deposition.

Thickness and composition of CdS cannot be measured using the current set-up. The Cd Kα emission is at a higher energy that the incident x-rays, and the Cd Lα emission is nearly indistinguishable (at the resolution of the current set-up) from the underlying In in the CIGS. Thus, the measurement of the amount of Cd present would require either a higher energy excitation, or a higher resolution detector. Additionally, the S emission borders on the detector's lower energy limit. Any use of XRF for CdS would necessarily be in a physical vapor, not chemical bath, deposition environment.

The use of XRF for thickness and composition measurements of ZnO or ITO on top of CIGS is also problematic. Zn emission overlaps strongly with Cu and Ga emissions. Measurements of the amount of Zn present would require either a higher resolution detector, or a careful deconvolution of the Zn, Cu, and Ga emissions, which is likely to decrease accuracy. In emission from the ITO will overlap with the significant In emission from the CIGS film. Sn emission can only be distinguished from In emission if a higher energy excitation is employed. Oxygen emission is below the lower energy limit of the current detector. Furthermore, oxygen vacancies at doping concentrations affect transparent conducting oxide (TCO) properties. Therefore even if a lower-energy detector was used, the measurement accuracy required for a useful to determination of TCO composition is prohibitive.

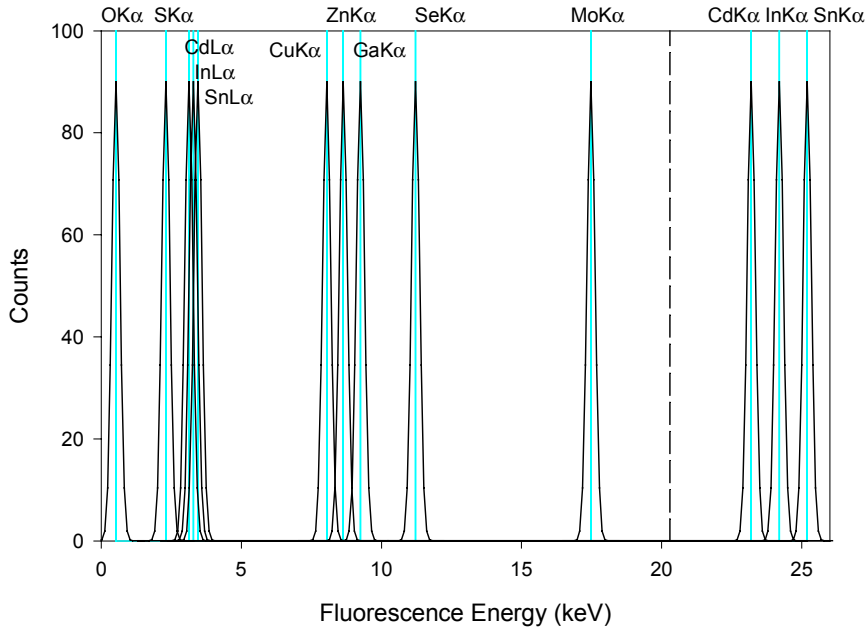

Figure 18: Fluorescence energies of major elements involved in CIGS modules.

Table 2 summarizes what information can be derived for each layer of the CIGS module using in-situ XRF on the film stack. The shaded column lists this information for the current XRF hardware. The column to the right of the shaded column lists the same information if one were to use higher-cost XRF hardware. The higher-cost XRF hardware would include at least one of the following, depending on the material's characteristics: 1) higher energy incident x-rays, 2) higher resolution, or 3) lower low-energy detection limit.

		CURRENT HARDWARE		HIGHER-COST HARDWARE	
	Appropriate to deposition environment	Thickness	Composition	Thickness	Composition
Layer:					
Mo	✔	✔	NA	✔	NA
CIGS	✔	✔	✔	✔	✔
CBD CdS	No	NA	NA	NA	NA
PVD CdS	✔	No	No	✔	✔
ZnO	✔	✔ (?)	No	✔	No (?)
ITO	✔	No	No	✔	No

Table 2 : Summary of applicability of in-situ XRF to various layers in the CIGS module.

5. Infrared Thermometry

5.1 Introduction

Substrate temperature is a critical parameter throughout the CIGS deposition. Typical laboratory CIGS deposition systems monitor substrate temperature carefully through the use of thermocouples on the

back of the substrate. Such a configuration is problematic for production systems, where substrates are constantly moving through the system. Although heater temperatures are commonly monitored, changes in deposition conditions may change the relationship between heater temperatures and the actual substrate temperatures. For flexible substrates, thermocouple temperature measurement is particularly problematic, since the low thermal mass of the substrate implies that contact with thermocouples actually changes the substrate temperature.

Thus, non-contact temperature measurement is desirable. Criteria for a useful non-contact temperature measurement were established based on typical CIGS operating conditions. It was determined that the sensor must have the following characteristics:

- Minimum measurement range of 200 ^{o}C to 700 ^{o}C, with ±10 ^{o}C accuracy,
- Ability to measure materials with unknown emissivities in the range of 0.05 to 1,
- Ability to survive 600 ^{o}C Se-containing ambient, and
- Low cost.

Off-the-shelf IR temperature measurement systems do not satisfy the above criteria. A large class of off-the-shelf systems requires sample emissivities to be both known and high (~>0.3). Certain commercially-available "two-color" sensors allow temperature measurement independent of emissivity. However, such systems typically provide valid data no lower in temperature than 450 ^{o}C, and they require use of bifurcated fiber optics that cannot withstand the necessary temperatures. The fiber optics' intolerance to elevated temperature stems both from the temperature rating of the fiber itself, and from the tendency of the lenses used to gather sufficient signal into the fiber to lose alignment due to thermal expansion.

A sensor satisfying the criteria for useful non-contact temperature measurement during CIGS deposition was designed. Preliminary measurements have confirmed the validity of the design. However, a number of items for development remain as future work, including full in-situ testing.

5.2 Principles of Operation

A low-cost, non-contact sensor was designed that simultaneously measures substrate temperature and emissivity. The sensor measures these quantities based on the changes in both magnitude and wavelength distribution of thermal radiation that occur with changes in temperature. Figure 19 shows the power density radiated, as a function of wavelength, at two different temperatures and emissivities. Also shown are the wavelength response regions for two different IR sensors. Calculations are according to Plank's law[18]. For a fixed emissivity, the magnitude of the thermal radiation increases with temperature. Measuring the amount of emitted radiation is the simplest non-contact IR temperature measurement, but requires assuming a known emissivity. The magnitude of the radiation is proportional to the emissivity. However, regardless of emissivity, thermal radiation shifts to shorter wavelengths as temperature increases. Thus, the ratio of the signals from the long- and short-wavelength sensors will indicate the temperature, regardless of the emissivity. The emissivity can then be calculated using the temperature and the magnitude of the overall radiation.

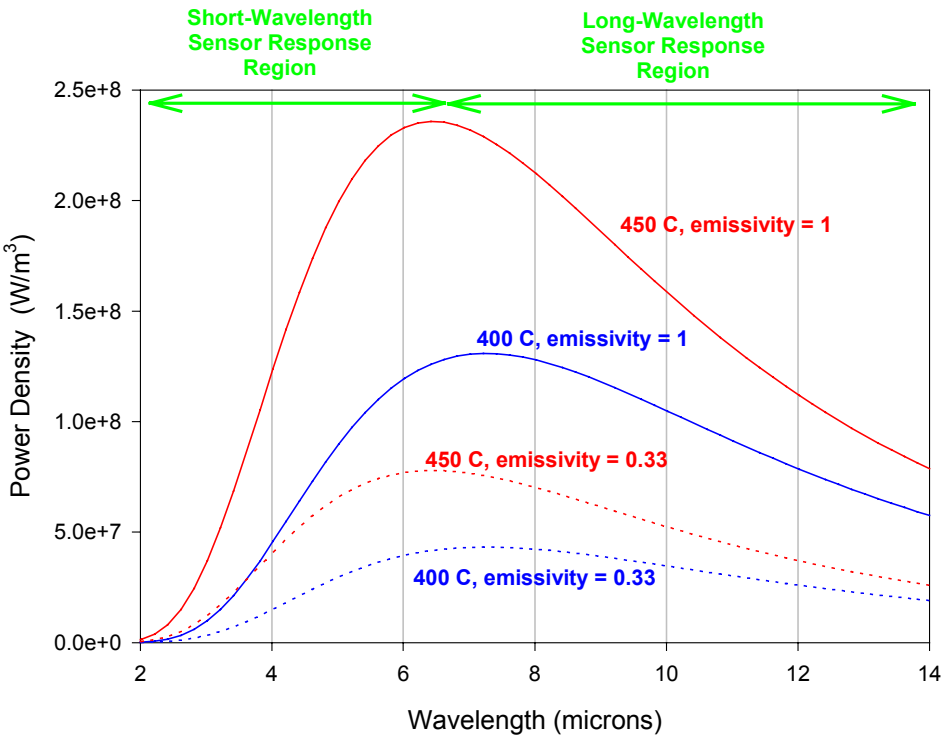

Figure 19: Magnitude and distribution of thermal radiation for two different emissivity bodies at two different temperatures. The wavelength response regions of two IR sensors are also shown.

The accuracy of the technique described above depends on the percent error in the signal from each sensor. Percent error increases as the signal decreases, either due to decreasing temperature, decreasing emissivity. Calculated uncertainty in temperature measurement, as a function of temperature, is shown by the red error bars of Figure 20. As the signal from each sensor increases at higher temperature, error decreases. The calculation assumes a typical 40 μV/°C response from each sensor, with 5 μV measurement error. The calculations shown are for an emissivity of 0.3. Error is smaller for higher emissivities (due to the larger signal), and larger for lower emissivities. The wavelength regions for each sensor are those pictured in the previous figure.

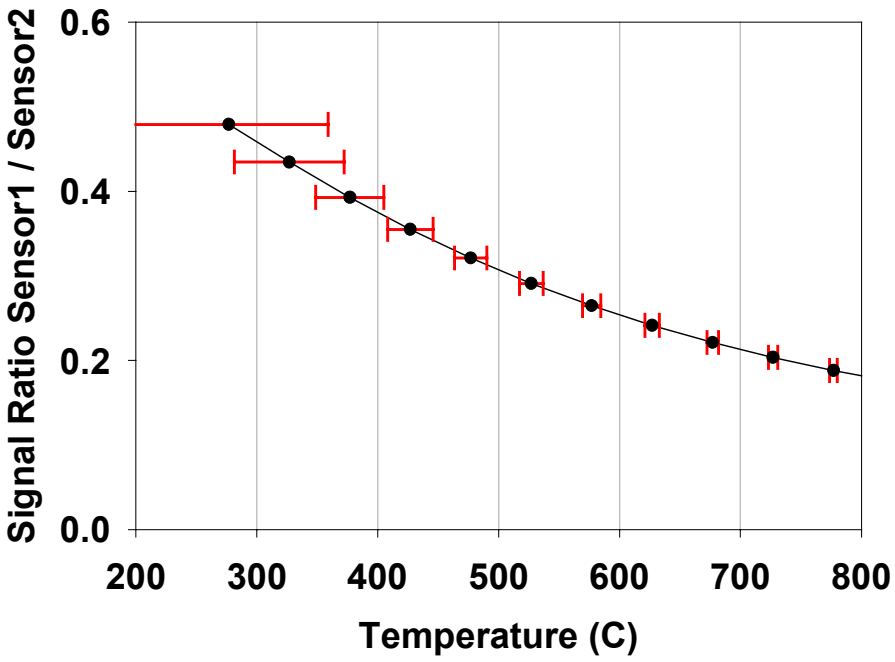

Figure 20: Error in derived temperature.

5.3 Equipment

Two IR sensors were purchased to cover approximately the wavelength regions illustrated in Figure 19. The sensors are commercially-available IR-sensitive thermopiles. The Omega 37-10-K ($437, response range 2-20 μm) is used to measure the contribution from the short- and long- wavelength response region, whereas the Omega 36-10-K ($375, response range 2-20 μm) is used to measure the contribution from the short- and long- wavelength response region. Each thermopile contains a thin piece of foil which increases in temperature based on the amount of incident IR radiation. Multiple low-mass thermocouples are mounted to the edge of the foil to measure its temperature increase. The sensors are named "IR thermocouples" by Omega, because the thermocouples internal to the sensor are connected with each other and with internal resistors to mimic conventional thermocouple output over some temperature and emissivity ranges. The sensor require no external power, as the signal is generated by the thermoelectric effect. The low-mass thermocouples have a significantly higher impedance (kΩ range) than traditional thermocouples, and therefore require a high-impedance voltmeter.

If the output of each sensor were specified as a function of incident power and wavelength, the relationship between the sensor signals and any sample temperature and emissivity could be calculated using variations of Plank's law. However, Omega does not provide such information, as the typical applications of these particular sensors deal only with variations in temperature, not emissivity. Therefore, it was necessary to define the response of each sensor as a function of wavelength and power. This was achieved using a cavity furnace of adjustable temperature and various apertures. The cavity furnace emits a blackbody spectrum, and its temperature was varied to change the spectral distribution incident on the sensors. The cavity furnace is a model ES1000-100 from Electro Optical Industries. The amount of radiation for a given distribution was varied using pie-shaped apertures. For a given temperature (spectral distribution) sensor output was found to be linear with aperture area.

Voltage from the sensors was measured using a high-impedance Keithley 2700 multi-channel multi-meter. Data was gathered from the meter via GPIB communication, and calculations were performed on a laptop computer.

5.4 Ex-Situ Results

Measurements were first performed ex-situ, on a hot plate, using samples with a variety of emissivities. Sample size was approximately 4" x 4". Sample temperature was monitored by a thermocouple attached to the sample edge. Samples were set on a 6" x 8" hot plate. IR sensors were attached to a ring stand to monitor the emission from a ~2" diameter spot at the sample center.

Figure 21 shows hot plate data for a ¼" thick Cu sheet. The circles indicate the thermocouple readout as a function of hot plate setting. The triangles show the temperature measured by the non-contact sensor. The +'s show the emissivity as measured by the non-contact sensor. Arrows after the first data point in each line indicate the order in which data points were taken. The sample visibly oxidized during the measurement. This oxidation is reflected in the increasing emissivity with time. In the literature,[19] polished Cu emissivity is quoted as 0.05, while that of completely oxidized Cu is quoted as 0.57.

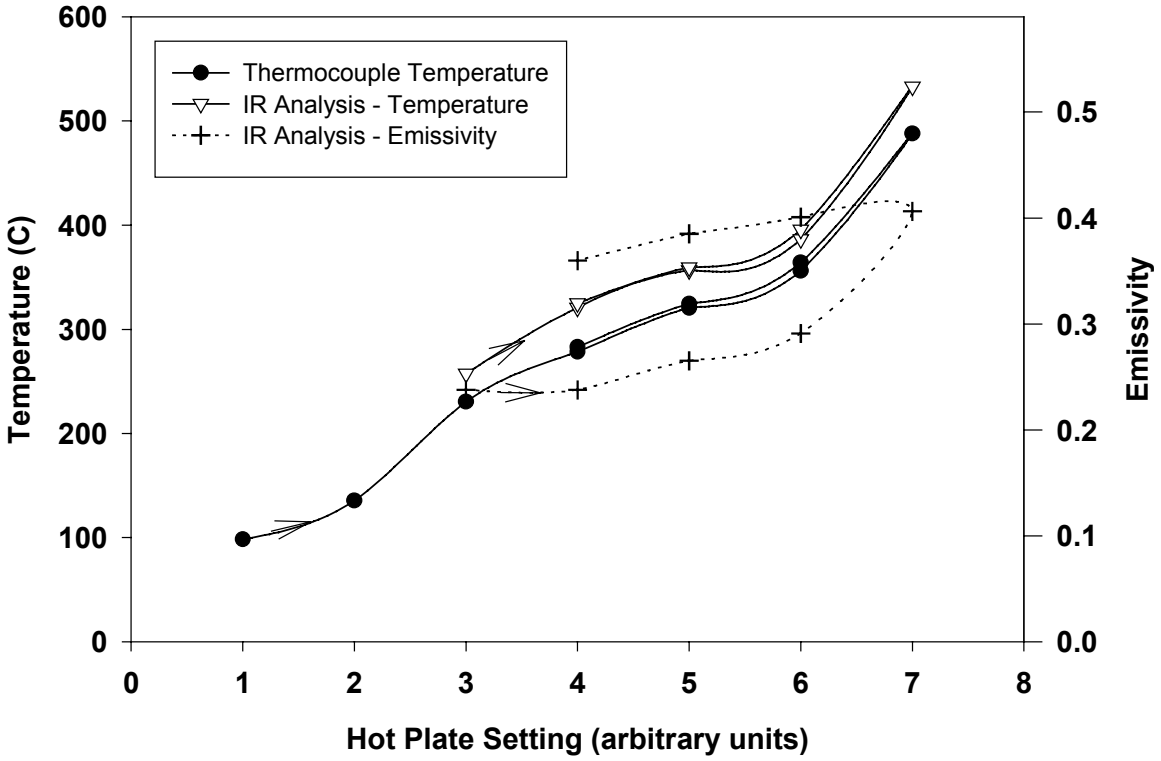

Figure 21: Temperature and emissivity of Cu plate as a function of hot plate setting.

A number of details require careful attention during measurements like that of Figure 21. The Omega sensors are significantly more sensitive to the sensor housing temperature than listed in the manufacture specifications. Thus, although the sensors can operate with housing temperatures close to 100 ^{o}C, the most accurate results are obtained when the sensors are cooled to temperatures close to room temperature, and signal from slight increases above room temperature are subtracted out. Second, the two IR detectors must be precisely positioned to look at the same area of the hot plate. If the hot plate temperature is spatially nonuniform and the sensors look at different areas, the percent error in the temperature uniformity propagates through the calculation to become several times larger in the results. Such error is compounded for surfaces that are nonuniform in emissivity.

There are two characteristics exhibited in Figure 21 that indicate sources of error in the measurement technique. First, the emissivity exhibits a slight temperature dependence after oxidation that must be an artifact of the measurement. Second, there is an offset between the temperatures measured by thermocouple and measured by IR thermometry. In fact, the coupling between the emissivity and temperature, and the temperature offsets, were much worse for the other materials measured. Figure 22 shows hot plate measurements made on steel, Al, glass, and Cu samples. For each sample, the thermocouple and IR thermometry temperatures track each other, but large offsets exist. Emissivities are not shown, but in each case were coupled with the sample temperature.

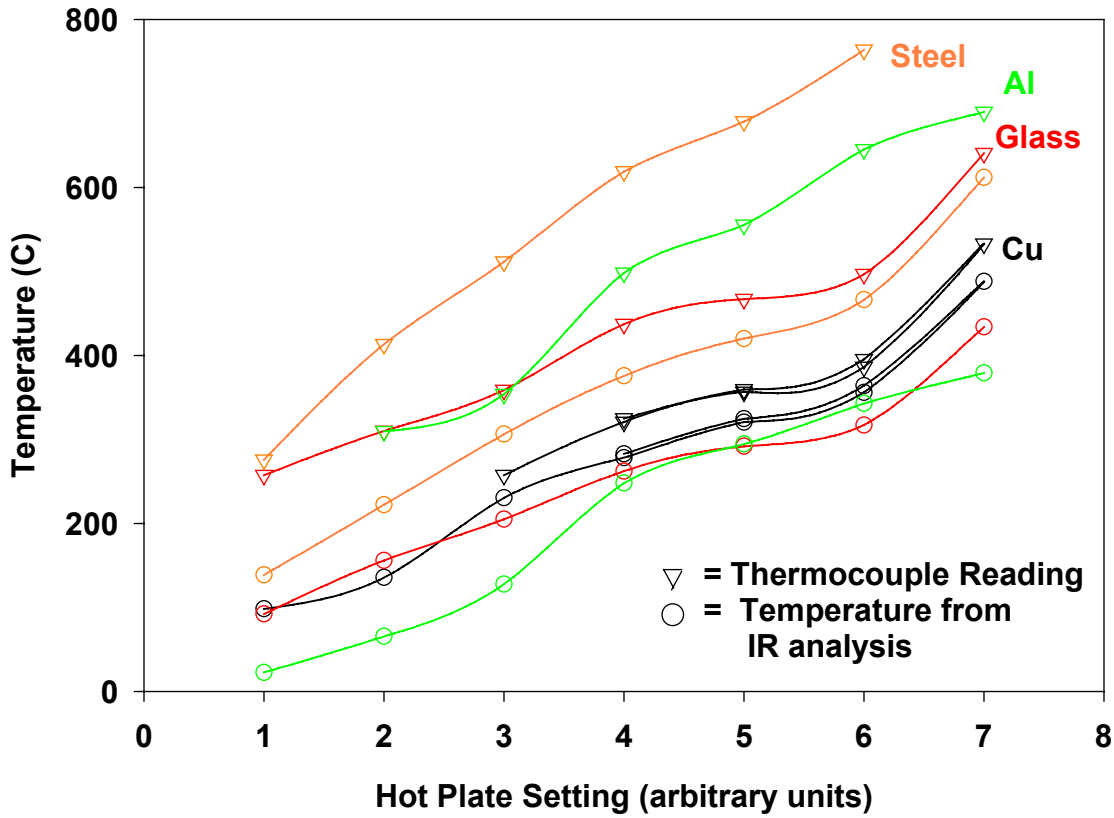

Figure 22: Temperature of a variety of sample types as a function of hot plate setting

The discrepancies of Figure 22 are likely explained by a wavelength-dependent emissivity. The IR sensors were calibrated with a black-body furnace having an emissivity of 1 over the entire spectral range of both sensors. If the emissivity of the test sample depends strongly on wavelength, this dependency will change the signal ratio between the two IR sensors.

If the wavelength-dependence of the test sample emissivity is known, it can be used to calculate the ratio between the average emissivities in the different wavelengths. This ratio is

$$c = \frac{\varepsilon_{os37}}{\varepsilon_{os36}}$$

where ε_{os36} = the average emissivity over the OS36 wavelength region

ε_{os37} = the average emissivity over the OS37 wavelength region

Values of c were varied for each sample until the emissivity and temperature were decoupled. The results are shown in Figure 23

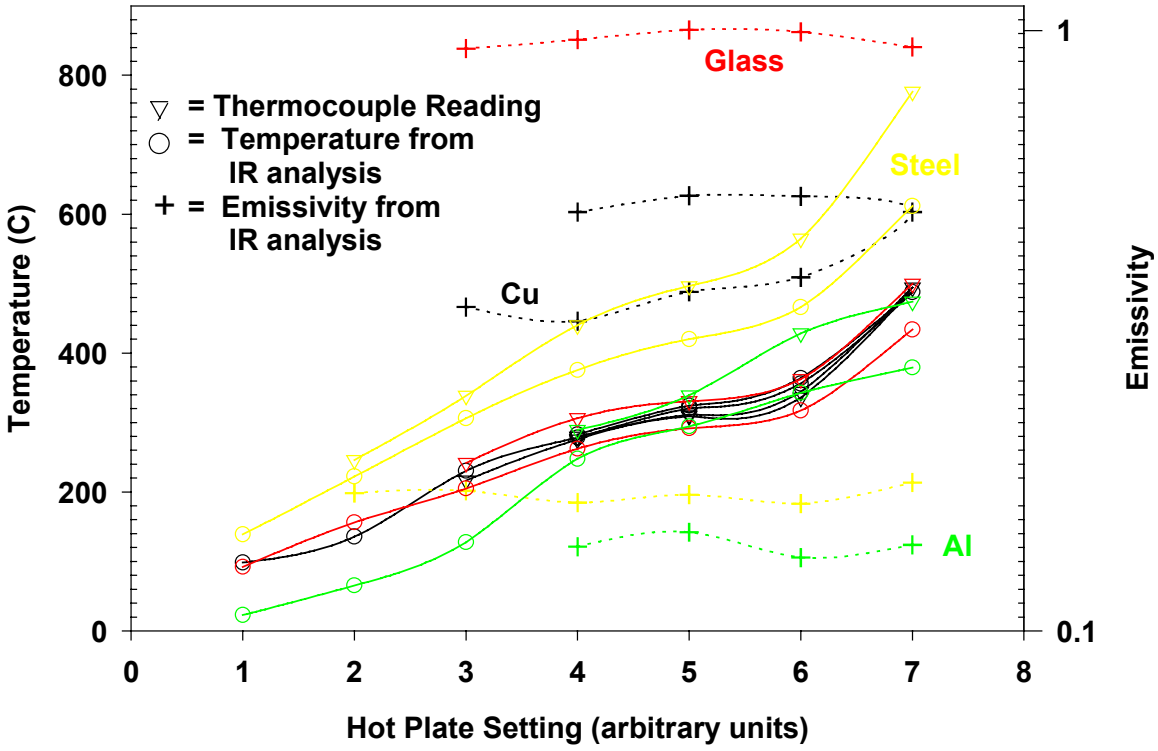

Figure 23: Temperature and emissivity of samples as a function of hot plate setting, after correcting for supposed variations in emissivity with wavelength.

When wavelength-dependent emissivity is taken into account, temperature offsets between the IR sensors and the thermocouple are reduced to a magnitude that could be accounted for by actual temperature difference between the thermocouple location and the IR spot. Also, emissivities are temperature-independent, and consistent with values quoted in the literature.[19] Table 3 compares the measured emissivity and accepted emissivity for each sample. Values of the ratio "c" needed to decouple emissivity and temperature for each sample are also shown.

Sample	C used for calculation	Measured emissivity	Accepted emissivity for polished surface	Accepted emissivity for oxidized surface
Cu	1.1	0.33-0.53	0.05	0.57
Glass	1.28	0.95	NA	0.85-0.95
Al	1.4	0.14	0.04-0.09	0.11-0.19
Steel	1.5	0.17	0.07	0.9-0.97

Table 3: Comparison of measured emissivity and accepted emissivity for each sample. Values of the ratio "c" needed to decouple emissivity and temperature for each sample are also shown.

The necessity to account for wavelength-dependent emissivity has several implications for the temperature measurement. First, it implies that calibration of IR sensors with the blackbody furnace may not be sufficient for accurate temperature measurement of all samples. The wavelength behavior of CIGS emissivity must be investigated. Second, to promote confidence in the non-contact measurement, the

emissivity as a function of wavelength for the samples listed above should be either measured or deduced from the literature. Characterization over the 2 – 20 μm wavelength range is required to verify the values of "c" used for calculation.

5.5 In-Situ Implementation

In-situ implementation of the IR thermometer requires several precautions. The sensor must be

- protected from Se,
- cooled adequately (kept below 100 ^{o}C),
- at a known temperature, so that output can be corrected for deviations from 25 ^{o}C, and
- screened from reflection from hot evaporation sources.

The above requirements are satisfied by the design shown in Figure 24. The OS-36 and OS-37 sensors are enclosed on all sides for protection from Se. The field of view of each sensor is shown as the light purple area. The sensors measure the substrate temperature through a ZnSe window, which has adequate transmission in the appropriate IR range, and is chemically stable at high temperatures. The ZnSe window is heated (if necessary) to drive off Se. A thermal break is placed between the ZnSe window and the rest of the enclosure to contain applied heat mostly to the window area. The sensors themselves are surrounded by water cooling coils. Thermocouples (shown as green in the figure) monitor the sensor temperatures and the temperature of the ZnSe window, as necessary for accurate data analyis. The signals from the sensors themselves are also carried in thermocouple wire pairs. The thermocouple wires exit the sensor enclosure through a cooled, baffled path. Such a path requires any Se vapor to undergo multiple collisions with cooled surfaces, and therefore prevents Se from entering the sensor enclosure. The use of a cooled inner area, a heated outer enclosure, and a window with thermal break is very similar to the design that was used successfully to implement XRF in-situ. A shield (shown as light blue) surrounds the measurement area. This shield is outside the field of view of the sensors, but it prevents radiation from the nearby hot evaporation sources from hitting the measurement area and being reflected into the sensors.

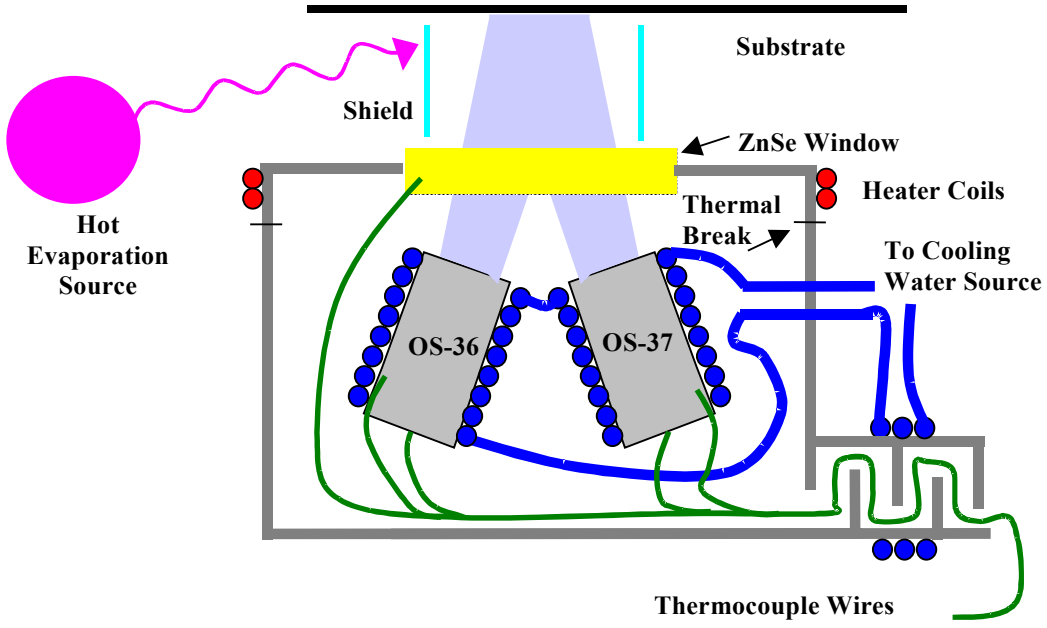

Figure 24: Schematic design of in-situ IR thermometer in cross-section. Schematic not drawn to scale.

The enclosure design of Figure 24 is expected to be effective, as it is very similar to the design that was used successfully to implement XRF in-situ. However, it has not yet been tested. As of the date of this report, the ZnSe windows have not arrived from the vendor.

5.6 Future Work with IR Thermometry

A number of items remain as future work in the development of the sensor described. First, for samples measured ex-situ, the wavelength-dependence of the emissivity should be measured by an independent technique. Such a determination is necessary the the behavior of the sensor for these samples is in fact well-understood. Second, full in-situ testing of the sensor must be performed. Such testing involves verifying that 1) the proposed design adequately protects the sensor from Se, 2) the emission from the ZnSe window can be removed from the signal, 3) the sensor is adequately cooled, and 4) reflections from heaters and sources are adequately screened from the sensor.

A further topic of investigation includes evaluation of this method for measuring evaporation source temperatures. One of the more straightforward aspects of such an investigation is choosing IR sensors with a response range that minimizes measurement error at much higher measurement temperatures. Perhaps the most difficult aspect to handle will be the necessary exposure of the sensor to nonvolatile compounds as it stares at the evaporation source. Metallic Cu and In that are likely to contaminate the sensor window can not be removed using the mild heating of the window (~200 ^{o}C) that is used to remove Se for a substrate temperature sensor.

6. OES investigations

OES has been used as an in-situ deposition monitor for a variety of sputtered materials, including ZnO,[20] ITO,[21] and CdS.[22] OES examines the light given off by species in the plasma that have been raised to excited states by electron impact. Excited species radiate at wavelengths corresponding to the quantum mechanically allowed transitions between electron energy levels. It is an attractive option for process control because it is fast, non-intrusive, can monitor multiple elements simultaneously, and provides information about deposition conditions in the plasma, not elsewhere in the chamber. OES is commonly used as an end point detector in plasma etching processes, where the disappearance of the etch product wavelength signature provides an unambiguous indication of completion. OES is only now beginning to be examined for controlling deposition processes, primarily because the dependence between OES signal and film properties can frequently be a quite complex function of the electron and gas densities, the emitting species concentration, the electron impact excitation cross section, the electron energy distribution function, and the probability of inelastic collisions between plasma species.

The evaluation of pulsed DC Se sputtering was proposed as a possible avenue to provide a high deposition rate, low-cost method of Se delivery that could be tightly controlled by OES. Pulsed DC sputtering was believed to hold promise in these areas because, at MRG, sputter rate from insulating targets of other materials has been increased many fold at a given cathode power by sputtering the target in a pulsed DC, rather than RF, mode. Additionally, the pulsed DC power supplies required to deposit at a given rate are much cheaper than their RF counterparts.

However, it was concluded that pulsed DC sputtering of Se is not an attractive option for manufacturable CIGS. Pulsed DC sputtering of Se was performed as a function of chamber pressure, source-to-substrate distance, cathode power, and target thickness. The experiments described above were performed at a fixed pulsing frequency of 20 kHz, as dictated by the available equipment. A DC plasma (no pulsing) could not be maintained using the Se target. The best deposition rate achieved by pulsed DC sputtering was 0.5 Å/sec. The effect of annealing the Se target in the presence of In and Ga was also investigated. Such anneals have been reported to affect the crystallinity and doping of the target, and hence the conductivity and maximum deposition rate[23]. However, no measurable increase in target conductivity or in deposition rate was observed. Furthermore, no Se emission lines were observable in the plasma. The

lack of detectable Se lines is presumably due to the small amount of Se in the plasma (i.e. small deposition rate), the absence of strongly emitting Se lines in the detectable range (240 to 1100 nm), and the strength of the Ar emissions.

OES was also considered for use during Cu, In, and Ga deposition. However, because OES control of these materials requires a plasma, OES is particular to less common deposition methods. Industrial partners indicating an interest in the in-situ sensors developed under the Thin Film Partnership Program were GSE, EPV, and OCLI, all of whom use non-plasma CIGS deposition. Therefore OES control of Cu, In, and Ga was not pursued.

7. Conclusions

In conclusion, several aspects of in-situ sensors for CIGS module deposition were explored. First, a composition sensor based on XRF was developed that

- Serves as a useful indicator of composition and thickness of CIGS,
- Contains only low-cost, commercially-available components,
- Has been verified for accuracy of both in-situ and ex-situ results,
- Has been exposed to over 600 hours of heated Se ambient without detriment,
- Was improved for a 20% increase in signal-to-noise on the second design iteration, and
- Has been used in closed-loop control of CIGS deposition.

The XRF sensor is clearly applicable to in-situ CIGS deposition, but is less appropriate for other layers in the module.

Second, non-contact IR thermometry was designed for substrate temperature and emissivity measurement during CIGS deposition. Preliminary measurements have confirmed the validity of the design. However, a number of items remain for future work, including full in-situ testing.

Finally, OES was considered for control of Se, Cu, In, and Ga rates, but was not pursued due to limited applicability.

8. Acknowledgements

A number of people contributed time and effort beyond that directly charged to this subcontract. Special thanks are deserved by Raghu Bhattacharya of NREL for ICP measurements, Lin Simpson of ITN for PDSE information, Dhirajlal Shah of GSE for SEM work, Robert Wendt and Doug Mason of GSE for assistance with equipment issues, and Jeff Britt of GSE for facilitating and advancing in-situ tests.

9. Publications and Presentations

The following publications and presentations were made as a result of the work described in this report:

1. Journal submission. I.L. Eisgruber, B. Joshi, N. Gomez, J. Britt, T. Vincent, "In-Situ X-Ray Fluorescence Used for Real-Time Control of $CuIn_xGa_{1-x}Se_2$ Thin Film Composition", submitted to *Thin Solid Films*, 7/9/01.
2. Seminar. "X-Ray Fluorescence and How it Applies to Control of $Cu(In,Ga)Se_2$ Deposition", ITN Energy Systems, 5/31/01.
3. Seminar. "Sensors Used in CIGS Module Deposition", ITN Energy Systems, 4/12/01.
4. Oral presentation and paper. I.L. Eisgruber, J.R. Engel, R.E. Treece, R.E. Hollingsworth, J. Britt, "In-Situ Measurements of $Cu(In,Ga)Se_2$ Composition by X-Ray Fluorescence", *Proceedings of the 28th IEEE Photovoltaics Specialists Conference*, pp. 505-508, (2000).

5. Poster presentation and paper. I.L. Eisgruber, J.R. Engel, R.E. Treece, R.E. Hollingsworth, "Results from the Development of a Low-Cost, In-Situ, $CuIn_xGa_{1-x}Se_2$ Composition Sensor Based on X-Ray Fluorescence", *Proceedings of the 2000 National Renewable Energy Laboratory Program Review Meeting*, pp. 255-256, (2000).
6. Poster presentation and paper. I.L. Eisgruber, T. Wangensteen, C. Marshall, B. Carpenter, "X-Ray Fluorescence as an In-Situ Composition Monitor During $CuIn_xGa_{1-x}Se_2$ Deposition", *American Institute of Physics Conference Proceedings*, **462**, 1998, pp. 138-143.

10. References

[1] G.T. Bush, M.D. Stebel, *Plating and Surface Finishing*, September 1983, 80-84, (1983).
[2] B.J. Cross, D.C. Wherry, *Thin Solid Films* **166**, 263-272, (1988).
[3] R. Muller, *Spectrochemical Analysis by X-Ray Fluorescence*, London: Adam Hilger, 1972, pg. 177.
[4] M. Murata, *X-Ray Spectrometry* **2**, 111-116 (1973).
[5] B. J. Mitchell, *Anal. Chem.* **32**, 1652-1657 (1960).
[6] J.W. Criss, L.S. Birks, *Anal. Chem.* **40**, 1080-1088 (1968).
[7] H.J. Beattie, R.M. Brissey, *Anal. Chem.* **26**, 980-989 (1954).
[8] R.J. Traill, G.R. Lachance, *Can. Spectrosc.* **11**, 63-69 (1966).
[9] R. Tertian, R. Vie le Sage, X-Ray Spectrom. 6, 123-130 (1977).
[10] W.K. de Jongh, *X-Ray Spectrom.* **2**, 151-158 (1973).
[11] R. Tertian, F. Claisse, *Principles of Quantitative X-Ray Fluorescence Analysis*, Heyden Publishing, pp. 51-69.
[12] J.W. Robinson, *CRC Handbook of Spectroscopy*, Vol. 1, 1974
[13] R. Tertian, F. Claisse, *Principles of Quantitative X-Ray Fluorescence Analysis*, Heyden Publishing, pp. 59-60.
[14] Ibid., pg 63.
[15] G.T. Bush, M.D. Stebel, "Measuring Plating Thickness with X-Ray Fluorescence", *Plating and Surface Finishing*, September 1983, pp. 80-84.
[16] R. Tertian, F. Claisse, *Principles of Quantitative X-Ray Fluorescence Analysis*, Heyden Publishing, pg. 64.
[17] L.J. Simpson, B.S. Joshi, L.A. Gonzales, J. Verley, T.E. Furtak, "A Parallel Detecting Spectroscopic Ellipsometer for Intelligent Process Control of Continuously Deposited CIGS Films", *Mater. Res. Soc. Symp. Proc.*, April 2000.
[18] See, for example, F. Reif, *Fundamentals of Statistical and Thermal Physics*, McGraw-Hill, 1965, pp. 386-388.
[19] Omega Corporation, "IRt/c Series OS36, OS37, OS38 Infrared Thermocouples, Operator's Manual", pg 5-1.
[20] M. Ruckh, D. Hariskos, U. Ruhle, H.W. Schock, "Applications of ZnO in $Cu(In,Ga)Se_2$ Solar Cells", *Proceedings of the 25th IEEE Photovoltaics Specialists Conference*, pp. 825-828, (1996).
[21] I.L. Eisgruber, J.R. Engel, R.E. Hollingsworth, P.K. Bhat, R. Wendt, "Intelligent Process Control of Indium Tin Oxide Sputter Deposition Using Optical Emission Spectroscopy", *Journal of Vacuum Science and Technology A*, **17(1)**, 1999, pp. 190-197.
[22] L. Wang, I. Eisgruber, R. Hollingsworth, C. DeHart, T. Wangensteen, R.E. Treece, P. Bhat, W. N. Shafarman, R. W. Birkmire, T.J. Gillespie, R. Wendt, "Manufacturable Large Area CdS Thin Films for Solar Cell Applications Monitored with Optical Emission Spectroscopy", *Mater. Res. Soc. Symp. Proc.*, **569**, 127-132, (1999).
[23] Dr. Frank Kustas, private communication, November 2, 1998.

REPORT DOCUMENTATION PAGE

Form Approved
OMB NO. 0704-0188

1. AGENCY USE ONLY (Leave blank)	2. REPORT DATE	3. REPORT TYPE AND DATES COVERED
	August 2001	Final Report August 15, 2001

4. TITLE AND SUBTITLE
In-Situ Sensors for Process Control of CuIn(Ga)Se_2 Module Deposition: Final Report, August 15, 2001

5. FUNDING NUMBERS
C: ZAK-8-17619-08
TA: PVP15001

6. AUTHOR(S)
I.L. Eisgruber

7. PERFORMING ORGANIZATION NAME(S) AND ADDRESS(ES)
ITN Energy Systems, Inc.
8130 Shaffer Parkway
Littleton, Colorado 80127-4107

8. PERFORMING ORGANIZATION REPORT NUMBER

9. SPONSORING/MONITORING AGENCY NAME(S) AND ADDRESS(ES)
National Renewable Energy Laboratory
1617 Cole Blvd.
Golden, CO 80401-3393

10. SPONSORING/MONITORING AGENCY REPORT NUMBER
NREL/SR-520-30870

11. SUPPLEMENTARY NOTES
NREL Technical Monitor: H.S. Ullal

12a. DISTRIBUTION/AVAILABILITY STATEMENT
National Technical Information Service
U.S. Department of Commerce
5285 Port Royal Road
Springfield, VA 22161

12b. DISTRIBUTION CODE

13. ABSTRACT *(Maximum 200 words)* This report describes several aspects of in-situ sensors for CIGs module deposition that were explored. First, a composition sensor based on X-ray fluorescence (XRF) was developed that serves as a useful indicator of composition and thickness of CIGS; contains only low-cost, commercially available components; has been verified for accuracy of both in-situ and ex-situ results; has been exposed to over 600 hours of heated Se ambient without detriment; was improved for a 20% increase in signal-to-noise on the second design iteration; and has been used in closed-loop control of CIGS deposition. The XRF sensor is clearly applicable to in-situ CIGS deposition, but is less appropriate for other layers in the module. Second, non-contract infrared thermometry was designed for substrate temperature and emissivity measurement during CIGS deposition. Preliminary measurements have confirmed the validity of the design. However, a number of items remain for future work, including full in-situ testing. Finally, optical emission spectroscopy was considered for control of Se, Cu, In, and Ga rates, but was not pursued due to limited applicability.

14. SUBJECT TERMS: PV; CuIn(Ga)Se_2 module deposition; in-situ sensors; X-ray fluorescence (XRF); optical emission spectroscopy (OES); infrared (IR) thermometry; atomic ratio; standard secondary fluorescence expression; isotropic emission

15. NUMBER OF PAGES

16. PRICE CODE

17. SECURITY CLASSIFICATION OF REPORT	18. SECURITY CLASSIFICATION OF THIS PAGE	19. SECURITY CLASSIFICATION OF ABSTRACT	20. LIMITATION OF ABSTRACT
Unclassified	Unclassified	Unclassified	UL